AIAA JOURNAL
Vol. 47, No. 9, September 2009

Acoustic Scattering by a Localized Thermal Disturbance

E. W. S. Kam,* R. M. C. So,† and R. C. K. Leung‡
Hong Kong Polytechnic University , Hong Kong, People's Republic of China

DOI: 10.2514/1.37398

Direct aeroacoustic simulation, which simulates acoustic radiation associated with unsteady fluid flows, involves capturing waves in both aerodynamic and acoustic scales. The presence of a thermal field further complicates this simulation. There are few analytical thermal-acoustic problems that could serve as benchmark to validate computational aeroacoustics schemes. This paper attempts to seek a theoretical solution of a simple problem involving scattering of acoustic plane waves by a localized zero-heat-gain/loss thermal disturbance and use it as a benchmark to verify the validity and extent of a numerical gas-kinetic scheme based on the modeled Boltzmann equation for the study of aeroacoustics resulting from thermal-flow/acoustic interaction. Two limiting cases with different acoustic wavelengths are attempted. Theoretical solutions are established for both cases, with the center of an axisymmetric thermal disturbance located at the origin of the physical domain. The incident acoustic wave has a dimensionless amplitude given by 1×10^{-4} and is propagated from left to right of the coordinate system. The simulation of the gas-kinetic scheme is carried out using the same computational setting as for the theoretical solutions. Riemann invariants are stipulated at the open boundaries. Numerical results are compared with the theoretical solutions and good agreement is obtained for the short-wavelength case only. The discrepancy for the long-wavelength case could be partially attributed to the inappropriateness of the Riemann invariants for oblique waves at the boundaries.

Nomenclature

a = sound speed
a_∞ = reference sound speed or characteristic velocity scale
D_n = dimension number
e = internal energy of fluid
$f(\mathbf{x}, \boldsymbol{\xi}, t)$ = particle distribution function
f_a = prescribed f at outlet boundary of the absorbing region
f^{eq} = equilibrium state of f
L = characteristic length scale
M = Mach number
Pr = Prandtl number
p = pressure
R = universal gas constant
Re = Reynolds number
r = radial coordinate
T = fluid temperature
t = time
u = x-direction velocity
$\mathbf{u}(u, v)$ = fluid velocity vector
v = y-direction velocity
v_r = radial velocity
v_ϕ = circumferential velocity
x = stream coordinate
$\mathbf{x}(x, y)$ = spatial vector
y = normal coordinate
Δt = time step
Δx = grid length along x
Δy = grid length along y
γ = specific heat ratio
κ = thermal conductivity
μ = first coefficient of viscosity
$\boldsymbol{\xi}$ = microscopic particle velocity vector
ρ = fluid density
σ = absorption coefficient
τ = collision relaxation time
ϕ = circumferential coordinate

Subscripts

i, j = indices for grid or velocity lattice
∞ = upstream condition

I. Introduction

IT HAS been more than a century since the first powered flight. Since then, the booming aviation industry and the abrupt growth of world population has contributed to the demand on air travel and on the rapid development of aviation, as well as the increasingly stringent restriction on community noise. With the advent of computers in the last several decades, active research in computational aeroacoustics (CAA) has been promoted to study and control noise generation associated with air transport. Numerical prediction of noise radiation associated with unsteady flows involves capturing waves in both aerodynamic and acoustic scales. In other words, propagation and interaction between three basic modes of motion in a slightly disturbed viscous heat-conducting gas [namely, acoustic (pressure), entropy (thermal), and vorticity (velocity) waves] are resolved in CAA studies [1].

In general, two major approaches to tackle aeroacoustic problems are commonly used in CAA studies: namely, hybrid or two-step method and direct aeroacoustic simulation (DAS) or one-step method [2]. The hybrid method resolves the unsteady compressible flow and the radiated sound field in two consecutive steps [3]. In this method, the interaction between the modes is not resolved. If the interaction between modes is to be studied, DAS is more appropriate because it can resolve every mode of interaction simultaneously. In reality, DAS involves solving a mixed set of scalar, vector, and tensor equations: that is, the state equation and the Euler or Navier–Stokes (NS) equations. The stringent requirements in temporal and spatial discretization lead to large computational cost. In view of this, effort has been made to simplify the numeric on simulating aeroacoustics

---

Received 3 March 2008; revision received 2 February 2009; accepted for publication 8 March 2009.

*Ph.D. Student, Department of Mechanical Engineering.

†Professor Emeritus, Department of Mechanical Engineering. Fellow AIAA.

‡Assistant Professor, Department of Mechanical Engineering; mmrleung@inet.polyu.edu.hk. Senior Member AIAA (Corresponding Author).

problems, which led to the exploration of an alternate numerical scheme based on the modeled Boltzmann equation (BE) [4]. In this approach, only scalar transport equations have to be solved and the solution yields all aerodynamic and acoustic scales simultaneously.

Among the three basic modes of motion, flow–sound interaction involved in the scattering of sound waves by vortices has received great attention. Numerous attempts have been made to study sound scattering by vortices, and the corresponding experimental, analytical, and numerical results are well documented [5–8]. According to Colonius et al. [8], the ratio of the incident acoustic wavelength to the size of the vortex is a critical parameter that has substantial effect on the scattered field. Two different limits are possible based on this ratio [9]. If the incident acoustic wavelength is small compared with the size of the vortex, it is referred to as the Wentzel–Kramers–Brillouin (WKB) limit, and it is referred to as the Born limit if the wavelength is large. According to Morse and Uno Ingard [7], scattered wave is defined as the wave given rise by the difference of two waves: one results from the interaction between the acoustic wave and the obstacle, and the other is the undisturbed wave in the absence of the obstacle. If scattering by an obstacle is close to the WKB limit, only half of the scattered wave spreads out in a near isotropic pattern from the obstacle, and the other half interacts with the incoming plane wave to form a sharp-edged shadow. On the other hand, if it is close to the Born limit, the scattered wave spreads out in all directions and no sharp-edged shadow is observed. If the wavelengths of the incoming acoustic waves lie between the two limits, different scattered fields can be obtained; these scattering results are known as the intermediate cases.

Study of sound scattering in the two limits has been carried out by various researchers. Georges [5] used high-frequency ray-tracing techniques for the WKB limit, and Müller and Matschat [6] considered the Born limit using a distributed vortex with velocity discontinuities. Their study was followed by the investigations of Ferziger [10], O'Shea [11], Howe [12], Yates [13], and Candel [14]. Numerical and analytical solutions of the NS equations were obtained by Colonius et al. [8] using distributed vortices with and without circulation. Furthermore, Ford and Llewellyn Smith [9] investigated the scattering of a plane acoustic wave by an axisymmetric vortex with localized vorticity, arbitrary circulation, and small Mach numbers.

Thermal-acoustic interaction has drawn much attention among researchers in the aerospace industry. This is due to the fact that instability can be introduced by a fluctuating transfer of heat [15] and a possible sound attenuation under favorable heat conditions [16]. The Rijke phenomenon [17], in which sound is generated by airflow through a sufficiently long vertical open-ended tube with a hot-wire net in its lower part, has been studied qualitatively by Rayleigh [18] and quantitatively by Landa [19]. Farouk et al. [20] numerically investigated a thermally induced acoustic wave in a two-dimensional cavity by either heating up or cooling down the vertical walls of the cavity. Most problems attempted to date were concentrated on thermal induced noise or computation of thermal effect on the absorption ability of air [16]. An exception is the study of Trilling [1], who showed that an instantaneous temperature rise due to an infinitely long plane wall could induce an acoustic wave.

Apart from the preceding cases, sound scattering due to thermal-acoustic interaction has not gained much attention, especially in a flowing medium. In view of this, an aeroacoustics problem with acoustic scattering from an axisymmetric localized heat source is studied in this paper. The theoretical solution of the acoustic scattering problem is first established as a benchmark. This is followed by a numerical simulation carried out by solving the modeled BE using the gas-kinetic scheme of Xu [21] and Xu and He [22].

II. Theoretical Analysis of Thermal-Acoustic Scattering

Scattering is a physical process whereby plane acoustic waves are forced to deviate from their straight trajectories by one or more localized obstacles residing in the medium through which they pass [7]. In the present thermal-acoustic interaction study, the localized obstacle is a thermal disturbance. It is constructed by structuring a weak temperature distribution, such that the net heat loss/gain would be zero in the absence of incident acoustic waves (similar to the case of a zero-circulation vortex, in which lift is absent). Consequently, the distributed heat source is stationary with respect to time.

The reasons for choosing such thermal disturbance are twofold. As mentioned in the Introduction, DAS should be able to resolve the interaction of aerodynamic and acoustic scales of the unsteady flow simultaneously. In general, the numerical requirement is more stringent in resolving the acoustic scale. Therefore, if a DAS numerical scheme is sufficiently accurate to properly resolve the flow interactions (e.g., scattering) at acoustic scale, it would have no problem in tackling the interaction with aerodynamic scale. This is the reason why the acoustic interaction of localized flow nonuniformities (e.g., acoustic, vorticity, and entropy pulses) is taken as the first benchmark problem for validation in previous DAS studies [4]. Another reason for this choice is that if the net heat gain/loss of the thermal disturbance is nonzero, heat transfer will occur and there will be an energy flow from the source located at the origin, even in the absence of the incident acoustic wave. This energy will introduce long-range effects on the scattering that might mask the actual thermal-acoustic interaction. In fact, according to Chu [23], a weak energy disturbance in a form similar to the present formulation makes the analysis of the interaction between acoustics and aerodynamic unsteadiness in a viscous compressible heat-conductive flow more manageable. This model for the thermal disturbance proved to be a viable benchmark problem for the present investigation. Furthermore, the thermal-acoustic scattering problem is amenable to an analytical steady-state solution; the sketch for this problem is shown in Fig. 1.

A. Localized Axisymmetric Thermal Disturbance

In the present analysis, the variables are made dimensionless using the following characteristic scaling parameters (dimensional quantities are denoted by an asterisk $*$): the length scale L is chosen to be the characteristic length of the obstacle, the speed of sound $a_\infty (a_\infty^2 = \gamma R T_\infty = \gamma p_\infty/\rho_\infty)$ is taken to be the velocity scale, the time scale is L/a_∞, the temperature scale is T_∞, and the density scale is ρ_∞. With these characteristic scaling parameters, the dimensionless density, temperature, and pressure are $\rho = \rho^*/\rho_\infty$, $T = T^*/T_\infty$, and $p = p^*/\rho_\infty a_\infty^2$, respectively. Unless otherwise specified, all quantities in the subsequent discussion are dimensionless.

In a quiescent environment, the axisymmetric heat source is governed by a set of time-independent nondimensional conservation laws; these are the conservation laws for mass, momentum, and energy. In 2-D polar coordinates (r and ϕ), they can be written as

$$\frac{\partial(\rho v_r)}{\partial r} + \frac{\rho v_r}{r} = 0 \tag{1}$$

$$\rho v_r \frac{\partial v_r}{\partial r} = -\frac{\partial p}{\partial r} + \frac{1}{Re_\infty}\left(\frac{\partial \sigma_{rr}}{\partial r} + \frac{\sigma_{rr}}{r}\right) \tag{2}$$

$$\begin{aligned}\rho v_r \frac{\partial e_t}{\partial r} &= -p\left(\frac{\partial v_r}{\partial r} + \frac{v_r}{r}\right) \\ &\quad + \frac{1}{Re_\infty}\frac{1}{Pr_\infty}\frac{1}{(\gamma-1)}\left(\frac{\partial^2 T}{\partial r^2} + \frac{1}{r}\frac{\partial T}{\partial r}\right) + Q(r) + \Phi\end{aligned} \tag{3}$$

$$p = \rho T/\gamma \tag{4}$$

where $Re_\infty = \rho_\infty a_\infty L/\mu$; $Pr_\infty = (c_p)_\infty \mu/\kappa$; $(c_p)_\infty$ is the specific heat capacity at constant pressure p_∞; σ_{rr} is the shear stress; e_t is the total energy (kinetic energy plus internal energy); $Q(r)$ is the dimensionless heat source; and Φ is the dimensionless work done due to viscous stress. In the case of the linearized Euler equations (LEE), the fluid is assumed to be inviscid. Therefore, viscous terms σ_{rr} and Φ vanish. The coefficient of the heat conduction term $1/\{Re_\infty Pr_\infty(\gamma-1)\}$ is reduced to $\kappa/\rho_\infty a_\infty L(c_p)_\infty(\gamma-1) = C$.

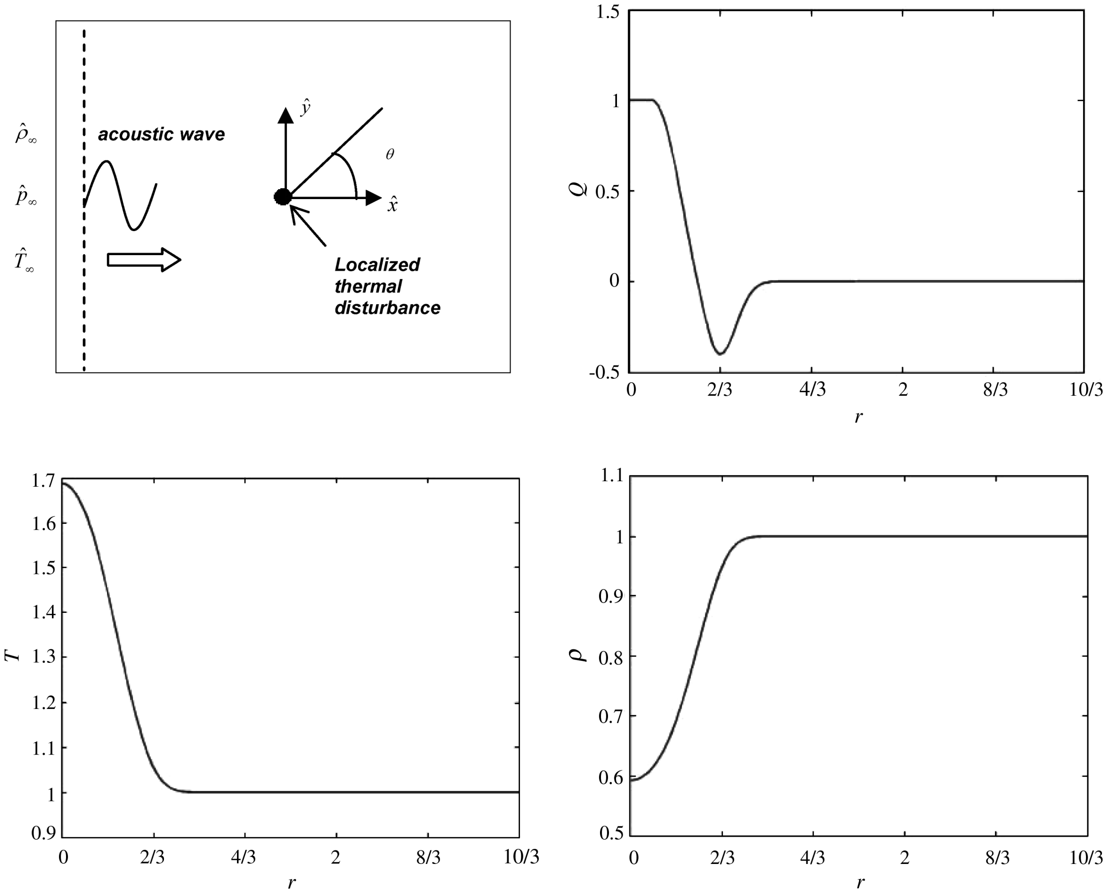

Fig. 1 Sketch of the acoustic scattering problem and the corresponding heat, temperature and density distributions of the thermal disturbance.

The steady-state solution of Eqs. (1–3) can be assumed to be given by

$$\bar{v}_r = 0; \qquad p = p_\infty = \frac{1}{\gamma}; \qquad T = \bar{T}(r)$$

$$\rho = \bar{\rho}(r) = \frac{p_\infty}{R\bar{T}(r)} = \frac{1}{\bar{T}(r)} \tag{5}$$

It can be shown that Eqs. (1) and (2) are identically satisfied and Eq. (3) is reduced to

$$C\frac{1}{r}\frac{\mathrm{d}}{\mathrm{d}r}\left(r\frac{\mathrm{d}(\bar{T}(r))}{\mathrm{d}r}\right) = -Q(r) \tag{6}$$

For a line heat source given by $Q(r) = C\delta(r)/4\pi r$ in an infinite domain, the solution of Eq. (6) leads to a $\ell n(r)$ term in $\bar{T}(r)$; therefore, $\bar{T}(r)$ will become unbounded as $r \to \infty$ and a steady-state solution cannot be obtained for a line heat source. To avoid divergence as $r \to \infty$, a distributed heat source with total source strength given by

$$\int_0^\infty Q(r) r \,\mathrm{d}r = 0 \tag{7}$$

is invoked. After some tedious algebra, the distributed heat source $Q(r)$ that satisfied Eq. (7) can be determined as (the corresponding distribution is shown in Fig. 1):

$$Q(r) = Q_1(r) = 1 \quad \text{for } r \le r_1 \tag{8a}$$

$$Q(r) = Q_2(r) = C_0 + (1 - C_0)e^{-\left(\frac{r-r_1}{b_1}\right)^2} \quad \text{for } r_1 \le r \le r_2 \tag{8b}$$

$$Q(r) = Q_3(r) = C_1\left(1 - e^{\left(\frac{r_3-r_2}{b_2}\right)^2-\left(\frac{r-r_3}{b_2}\right)^2}\right) \quad \text{for } r_2 \le r \le r_3 \tag{8c}$$

$$Q(r) = Q_4(r) = C_3 e^{\left(\frac{r_3-r_2}{b_2}\right)^2-\left(\frac{r-r_3}{b_3}\right)^2} \quad \text{for } r_3 \le r \tag{8d}$$

where $r_1 = 1/6$, $r_2 = 1/2$, $r_3 = 2/3$, $b_1 = 1.0$, $b_2 \approx 0.6401$, $b_3 = 0.5$, $C_0 = e^{-1}/(e^{-1} - 1) \approx 0.5820$, $C_1 \approx 0.4769$, and $C_3 \approx 0.2178$. To visualize sound scattering by this axisymmetric heat source, $Q(r)$ is taken to be bounded at $r = 1.0$. The corresponding temperature distribution and density distribution are determined by Eq. (6) and $\bar{\rho} = \bar{\rho}(r) = 1/\bar{T}(r)$; their respective distributions are shown in Fig. 1.

B. Scattering by a Localized Thermal Disturbance

In the absence of acoustic waves, the mean thermal field due to a localized axisymmetric thermal disturbance is given by Eq. (5) plus the condition $\bar{v}_\phi = 0$. The acoustic field may be derived using the LEE approach with the additional assumption that the localized thermal disturbance is not affected by the incident acoustic waves. In other words, the nonlinear interaction between the incident sound waves and the axisymmetric thermal disturbance is assumed to be negligible. In 2-D polar coordinates, the conservation laws for the fluctuating macroscopic properties (ρ, v_r, v_ϕ, and p) in the LEE can be expressed as

$$\frac{\partial \rho}{\partial t} + \bar{\rho}\frac{\partial v_r}{\partial r} + v_r\frac{\partial \bar{\rho}}{\partial r} + \bar{\rho}\frac{v_r}{r} + \frac{\bar{\rho}}{r}\frac{\partial v_\phi}{\partial \phi} = 0 \tag{9}$$

$$\bar{\rho}\frac{\partial v_r}{\partial t} = -\frac{\partial p}{\partial r} \tag{10}$$

$$\bar{\rho}\frac{\partial v_\phi}{\partial t} = -\frac{1}{r}\frac{\partial p}{\partial \phi} \tag{11}$$

$$\frac{\partial p}{\partial t} + \left(\frac{\partial v_r}{\partial r} + \frac{v_r}{r} + \frac{1}{r}\frac{\partial v_\phi}{\partial \phi}\right) = 0 \tag{12}$$

For a monochromatic incident acoustic wave with nondimensional frequency ω, the separation-of-variable technique can be used to factor out the time dependence. Consequently, the real part of ρ, v_r, v_ϕ, and p can be expressed as

$$\begin{bmatrix} \rho \\ v_r \\ v_\phi \\ p \end{bmatrix} = \Re\left\{\begin{bmatrix} \hat{\rho}(r,\phi) \\ \hat{v}_r(r,\phi) \\ \hat{v}_\phi(r,\phi) \\ \hat{p}(r,\phi) \end{bmatrix} e^{-i\omega t}\right\} \tag{13}$$

where $\hat{\rho}$, $\hat{v}_r$, $\hat{v}_\phi$, and $\hat{p}$ are the total fluctuation amplitudes of density, velocity, and pressure, respectively. Equations (10–12) form a closed system and $\hat{v}_r$, $\hat{v}_\phi$, and $\hat{p}$ are

$$\hat{v}_r = \frac{1}{i\omega\bar{\rho}}\frac{\partial \hat{p}}{\partial r} \tag{14}$$

$$\hat{v}_\phi = \frac{1}{i\omega\bar{\rho}r}\frac{\partial \hat{p}}{\partial \phi} \tag{15}$$

$$-i\omega\hat{p} + \left(\frac{\partial \hat{v}_r}{\partial r} + \frac{\hat{v}_r}{r} + \frac{1}{r}\frac{\partial \hat{v}_\phi}{\partial \phi}\right) = 0 \tag{16}$$

where $\hat{\rho}$ can be determined subsequently by substituting the solution of $\hat{v}_r$, $\hat{v}_\phi$, and $\hat{p}$ into Eq. (9). A single equation for $\hat{p}$ can be obtained by substituting Eqs. (14) and (15) into Eq. (16); the result is

$$\frac{\partial^2 \hat{p}}{\partial r^2} + \left(\frac{1}{r} - \frac{1}{\rho}\frac{\mathrm{d}\rho}{\mathrm{d}r}\right)\frac{\partial \hat{p}}{\partial r} + \frac{1}{r^2}\frac{\partial^2 \hat{p}}{\partial \phi^2} + \rho\omega^2\hat{p} = 0 \tag{17}$$

As $r \to \infty$ and $\rho \to \rho_\infty$, Eq. (17) can be written as

$$\frac{\partial^2 \hat{p}}{\partial r^2} + \omega^2\hat{p} = 0 \tag{18}$$

For a plane incident wave with amplitude A propagating in the x direction, the incident pressure in 2-D polar coordinates can be written as

$$\hat{p}_i = Ae^{i\omega r\cos\phi} = A\sum_{m=0}^{\infty} i^m \varepsilon_m J_m(\omega r)\cos m\phi \tag{19}$$

where $J_m(\omega r)$ is the Bessel function of order m, $\varepsilon_0 = 1$, and $\varepsilon_m = 2$ for $m = 1, 2, 3, \ldots$. The solution for $\hat{p}$ in Eq. (19) in the r range, $0 < r < \infty$, can be obtained in three regions as follows:

1. *Solution for $\hat{p}$ in Region I ($0 < r \le r_1$ with $r_1 \ll 1/3$)*

Suppose that $\hat{p}_s$ are the scattered waves. The solution for Eq. (17) can therefore be expanded in a Fourier series as

$$\hat{p} = \hat{p}_i + \hat{p}_s = \sum_{m=0}^{\infty} D_m g_m(r)\cos m\phi \tag{20}$$

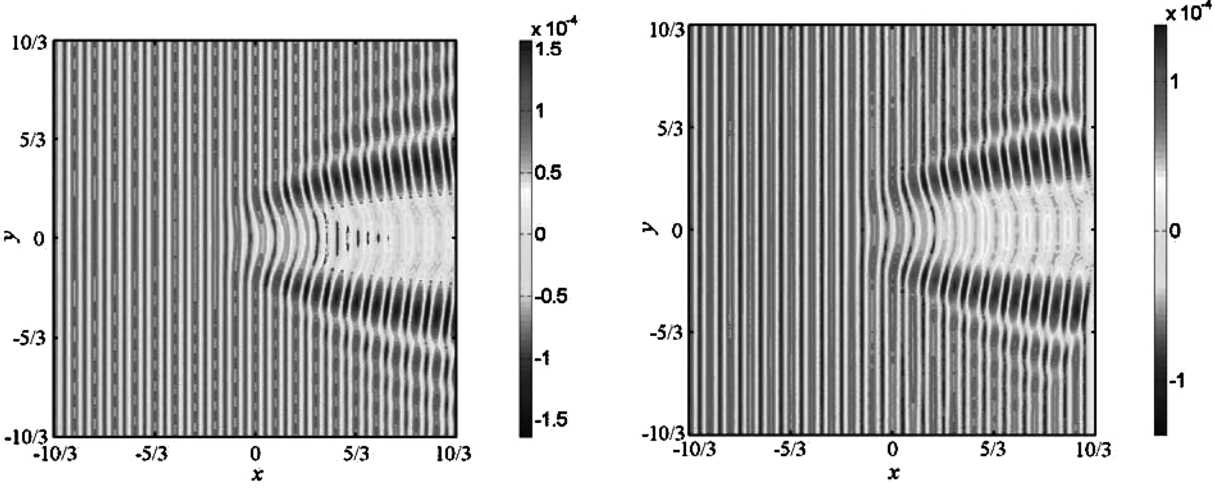

a) Theoretical solution

b) Gas-kinetic scheme result

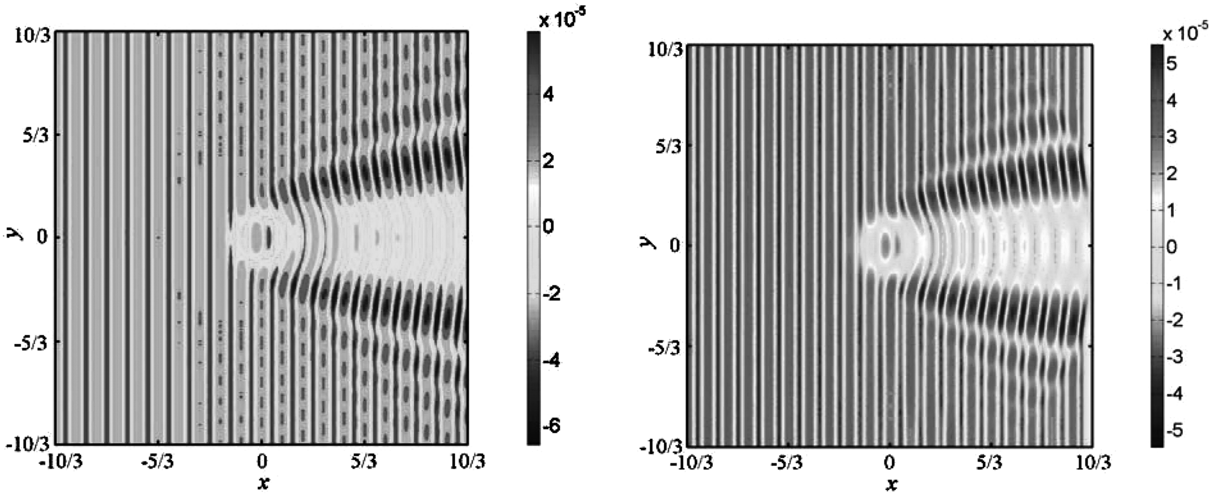

c) Theoretical solution

d) Gas-kinetic scheme result

Fig. 2 Interaction between thermal disturbance and acoustic wave for the $\lambda = 1/3$ case. Top row: total pressure fluctuation amplitude $\hat{p}$; bottom row: total temperature fluctuation amplitude $\hat{T}$.

To determine $g_m(r)$, Eq. (20) is substituted into Eq. (17), with the coefficient of the Fourier cosine series set to zero. The result is

$$\frac{\mathrm{d}^2 g_m}{\mathrm{d}r^2} + \left(\frac{1}{r} - \frac{1}{\bar{\rho}}\frac{\mathrm{d}\bar{\rho}}{\mathrm{d}r}\right)\frac{\mathrm{d}g_m}{\mathrm{d}r} + \left(\rho\omega^2 - \frac{m^2}{r^2}\right)g_m = 0 \tag{21}$$

where g_m must be finite as $r \to 0$. In region I, Eq. (21) is further reduced to

$$\frac{\mathrm{d}^2 g_m}{\mathrm{d}r^2} + \frac{1}{r}\frac{\mathrm{d}g_m}{\mathrm{d}r} + \left(\omega_0^2 - \frac{m^2}{r^2}\right)g_m = 0 \tag{22a}$$

where $\omega_0^2 = \rho(0)\omega^2$, with the solution for g_m expressed as

$$g_m(r) = r^m \tag{22b}$$

which is used as the starting value for marching the solution from $r = r_1$ to r_2. Note that the arbitrary constant is set to unity in this solution for g_m; its deviation from unity is absorbed into the coefficient D_m, which has to be determined.

2. *Solution for $\hat{p}$ in Region II ($r_1 < r \leq r_2$ with $r_2 \geq 1$)*

In this region, r_2 is taken to be greater than (but close to) 1.0, where the thermal disturbance is localized at $r \leq 1$ and the density is essentially at its uniform value outside this region. Again, $\hat{p}$ can be expressed as Eq. (20) and g_m is obtained by solving Eqs. (21) and (22).

3. *Solution for $\hat{p}$ in Region III ($r_2 < r < \infty$)*

In this region, the scattered waves should be an outgoing wave, which can be expressed as

$$\hat{p}_s = A\sum_{m=0}^{\infty} i^m \varepsilon_m g_m(r)\cos m\phi \tag{23}$$

where

$$g_m = B_m H_m^{(1)}(\omega r)$$

Here, B_m is a constant to be determined for every mode and $H_m^{(1)}$ is the Hankel function of the first kind [24]. Therefore, $\hat{p}$ in Eq. (17) is in the form

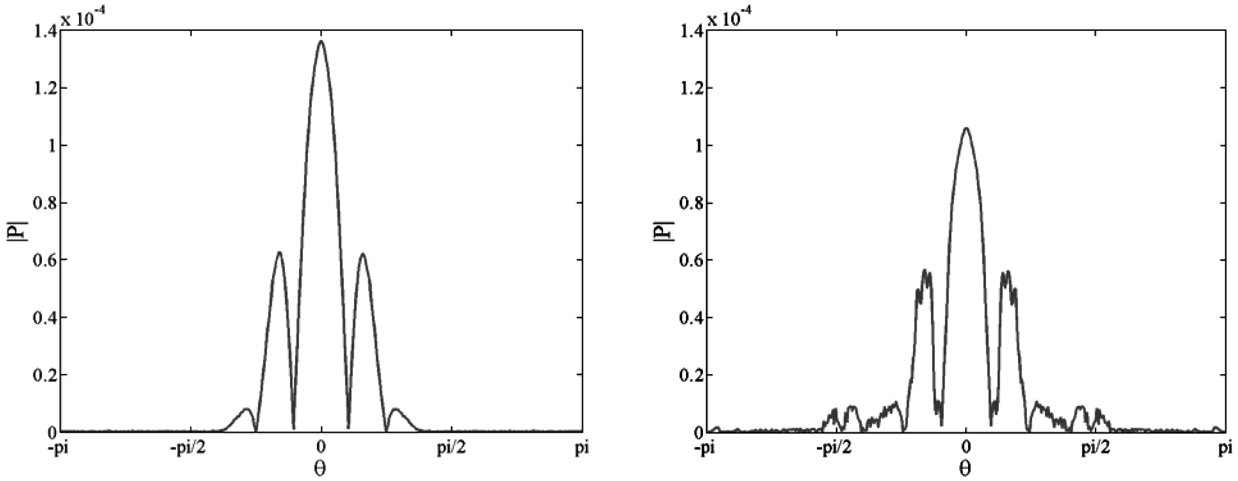

a) b)

Fig. 3 Circumferential variations of scattered-pressure fluctuation amplitude at $r/\lambda = 7$ for the $\lambda = 1/3$ case: a) theoretical solution and b) gas-kinetic scheme result.

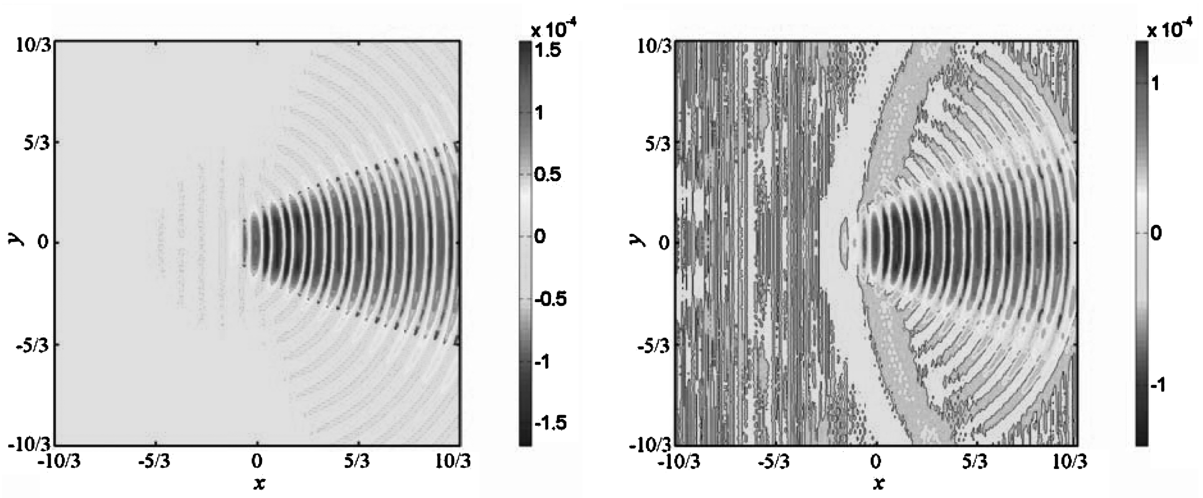

a) b)

Fig. 4 Distribution of scattered-pressure amplitude $\hat{p}_s$ for the $\lambda = 1/3$ case: a) theoretical solution and b) gas-kinetic scheme result.

$$\hat{p} = \hat{p}_i + \hat{p}_s = A \sum_{m=0}^{\infty} i^m \varepsilon_m [J_m(\omega r) + B_m H_m^{(1)}(\omega r)] \cos m\phi \quad (24)$$

Because $\bar{\rho}(r) \approx \rho_\infty$ in this region, Eq. (21) is reduced to

$$\frac{\mathrm{d}^2 g_m}{\mathrm{d}r^2} + \frac{1}{r}\frac{\mathrm{d}g_m}{\mathrm{d}r} + \left(\omega_1^2 - \frac{m^2}{r^2}\right) g_m = 0 \quad (25)$$

where $\omega_1^2 = \rho(r_2)\omega^2$ at $r = r_2$, thus providing an initial condition for the determination of B_m.

4. Patching of Solutions for $\hat{p}$ at $r = r_2$

The solution of $\hat{p}$ in Eq. (17) can be determined by patching the corresponding solutions obtained in region II and region III at $r = r_2$, where r_2 is defined such that $\rho = \bar{\rho}(r_2) \approx \rho_\infty$. Combining Eqs. (20) and (24), $\hat{p}$ becomes

$$\hat{p} = \hat{p}_i + \hat{p}_s = \begin{cases} \sum_{m=0}^{\infty} D_m g_m(r) \cos m\phi & r \le r_2 \\ A \sum_{m=0}^{\infty} i^m \varepsilon_m [J_m(\omega r) + B_m H_m(\omega r)] \cos m\phi & r \ge r_2 \end{cases} \quad (26)$$

At $r = r_2$, g_m and $\mathrm{d}g_m/\mathrm{d}r$ should be continuous, and the coefficients on the left-hand side and right-hand side of the cosine series should be equal for every mode. Therefore, for $0 \le m < \infty$,

$$D_m g_m = i^m \varepsilon_m A (J_m(\omega r) + B_m H_m^{(1)}(\omega r)) \quad (27)$$

$$D_m \frac{\mathrm{d}g_m}{\mathrm{d}r} = i^m \varepsilon_m A \left(\frac{\mathrm{d}J_m(\omega r)}{\mathrm{d}r} + B_m \frac{\mathrm{d}H_m^{(1)}(\omega r)}{\mathrm{d}r} \right) \quad (28)$$

To evaluate g_m, the initial value problem is solved numerically using a fourth-order Runge–Kutta scheme. At $r = r_1$, the solutions of g_m and $\mathrm{d}g_m/\mathrm{d}r$ are obtained from Eq. (22b) and are used as initial values for patching at $r = r_2$.

At $r = r_2$, both the Bessel function and the Hankel function can be determined, and so the unknown constants B_m and D_m are computed for every mode by solving Eqs. (27) and (28). The result is

$$B_m = \frac{(J_m'(\omega r) \cdot \omega \cdot g_m - J_m(\omega r)(\mathrm{d}g_m/\mathrm{d}r))}{H_m^{(1)}(\omega r)(\mathrm{d}g_m/\mathrm{d}r) - H_m^{(1)}(\omega r) \cdot \omega \cdot g_m} \quad (29)$$

$$D_m = \frac{i^m \varepsilon_m A[(J_m \cdot H_m^{(1)}(\omega r) \cdot \omega - J_m' \cdot \omega \cdot H_m^{(1)}(\omega r))]}{g_m H_m^{(1)}(\omega r) \cdot \omega - (\mathrm{d}g_m/\mathrm{d}r) H_m^{(1)}(\omega r)} \quad (30)$$

The corresponding g_m is therefore determined for every mode ($0 \le m < \infty$), and the pressure distribution $\hat{p}(r)$ can be calculated.

III. Numerical Solution Based on the Modeled Boltzmann Equation

In general, a DAS problem can be described by macroscopic measurable properties such as density, velocity, and pressure through a set of unsteady compressible NS equations. The success of solving an aeroacoustic problem using a modeled BE therefore depends greatly on its ability to resolve all macroscopic information embodied in such a problem.

The modeled BE is commonly represented by the Bhatnagar–Gross–Krook (BGK) model, with its dimensionless form given by [4]

$$\frac{\partial f}{\partial t} + \boldsymbol{\xi} \cdot \nabla f = -\frac{1}{\tau}(f - f^{\mathrm{eq}}) \quad (31)$$

where τ is the time taken for f to relax from a nonequilibrium state to a Maxwellian–Boltzmann equilibrium state f^{eq}. The BGK model is initially adopted for monatomic gases only. To apply it to diatomic gases for realistic aeroacoustic problems, Li et al. [4] proposed a two-relaxation-time model, in which both the translational and rotational degrees of freedom D_T and D_R in particle–particle collisions are taken into account. A set of unsteady compressible NS equations for diatomic gas is recovered by invoking the Chapman–Enskog (CE) expansion in terms of the Knudsen number Kn and with the macroscopic variables required for describing an aeroacoustic problem expressed as integral moments of f,

$$\int f \,\mathrm{d}\boldsymbol{\xi} = \rho \quad (32a)$$

$$\int \xi_i f \,\mathrm{d}\boldsymbol{\xi} = \rho u_i \quad (32b)$$

$$\frac{D_T + D_R}{D_T} \int \frac{1}{2} |\boldsymbol{\xi}|^2 f \,\mathrm{d}\boldsymbol{\xi} = \rho e + \frac{1}{2}\rho |u|^2 \quad (32c)$$

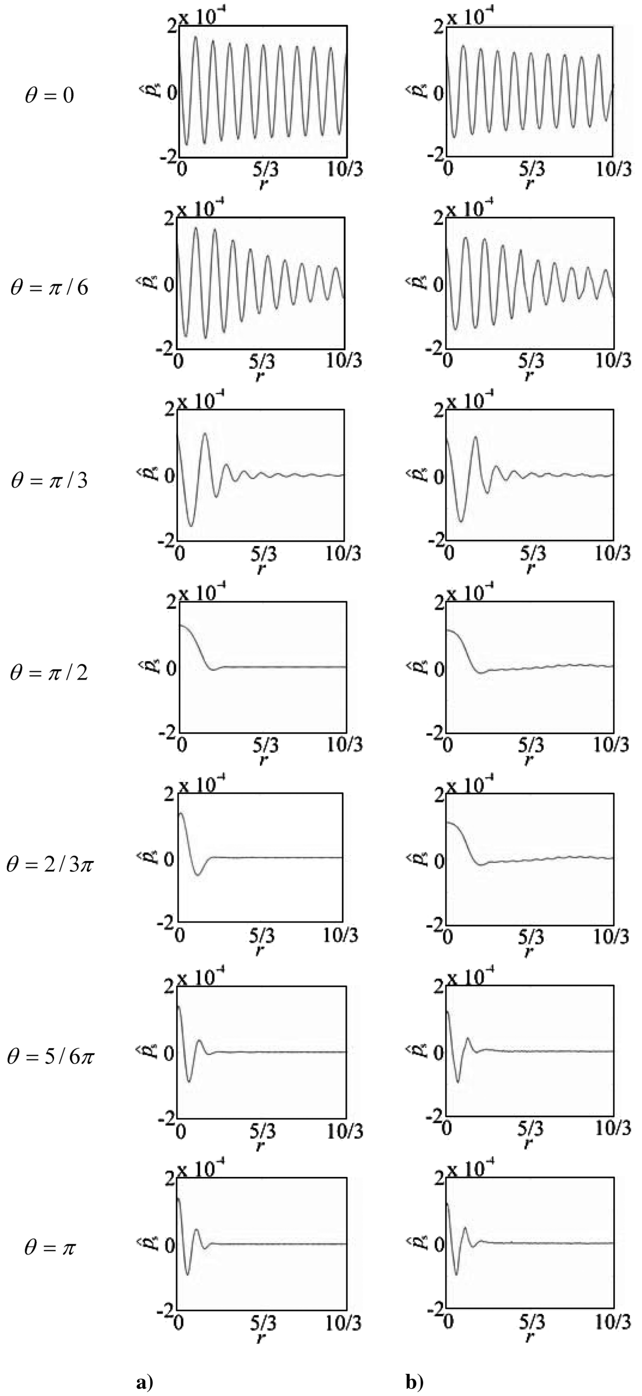

a) b)

Fig. 5 Radial variations of scattered-pressure fluctuation amplitude $\hat{p}_s$ for the $\lambda = 1/3$ case ($\hat{p}_s$ against r, with $-2 \times 10^{-4} \le \hat{p}_s \le 2 \times 10^{-4}$ and $0 \le r \le 10/3$): a) theoretical solution and b) gas-kinetic scheme result.

$$\frac{D_T + D_R}{D_T}\int \frac{1}{2}\xi_i|\boldsymbol{\xi}|^2 f\,\mathrm{d}\boldsymbol{\xi} = \left(\rho e + \frac{1}{2}\rho|u|^2 + p\right)u_i \tag{32d}$$

and the pressure is given by Eq. (4).

Invoking the CE expansion, the unsteady compressible NS equations are recovered with two limitations. First, τ is locally fixed in the BGK model. Physically, it should vary with the molecular velocity, which is directly related to the temperature. From the kinetic theory point of view, τ is an important parameter for a correct derivation of the equation of state for a diatomic gas or the specific heat ratio γ. Further, it is also important to correctly recover the transport coefficients, the first and second coefficients of viscosity μ and λ, and the thermal conductivity κ. To replicate the correct physics of a DAS problem using a modeled BE, a physical model based on Sutherland's law was invoked by Li et al. [4] so that τ varies with temperature, thus allowing the transport coefficient μ to be recovered correctly.

Second, the thermal conductivity κ, or its dimensionless counterpart Pr, thus derived was found to give rise to the condition $Pr = 1$. This value is not consistent with experimental data for real gases. For example, Pr should have a value of $2/3$ for a monatomic gas and $7/5$ for a diatomic gas. Physically, the incorrect value of Pr implies that the thermal energy exchange between particles has not been replicated properly. To simulate DAS problems correctly, the BGK model was further improved by Leung et al. [25] by invoking the Eucken model of heat conduction. A correct value of κ is obtained such that the thermal energy exchange during the collision process is partially taken into account.

A. Gas-Kinetic Scheme for Two-Dimensional Problems

Two numerical schemes are available for solving the modeled BE: namely, the lattice Boltzmann method (LBM) and the gas-kinetic scheme. Although LBM was adopted in Li et al.'s two-relaxation-time model [4] to study aeroacoustics problems, the improved modeled BE can be solved using different numerical schemes, as it is based on fundamental physical consideration; that is, the improved modeled BE can also be solved by the gas-kinetic scheme. To illustrate this, the numerical solution for the present thermal-acoustic scattering problem is obtained by a gas-kinetic scheme. In the following, a brief description of the gas-kinetic scheme proposed by Xu [21] is presented. Further details are available from Xu and He [22].

The gas-kinetic scheme adopted for the present numerical simulation of acoustic scattering by a localized thermal disturbance is based on the formulation given by Su et al. [26] and Xu and He [22]. The gas-kinetic BGK scheme is a finite volume scheme from which the mass, momentum, and energy fluxes are calculated across numerical cell interfaces. In Xu and He's model [22], the energy equation was not solved because the formulation was intended for

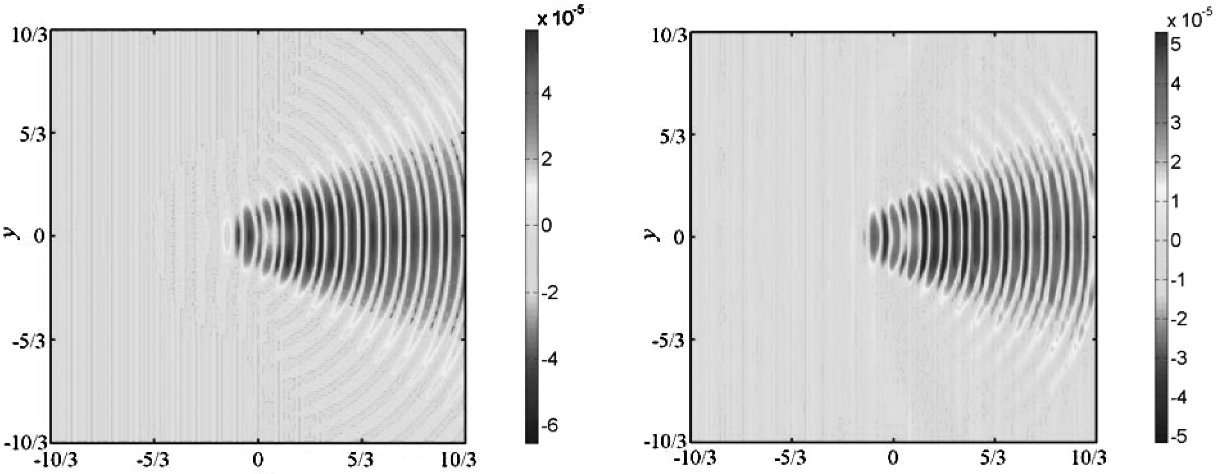

a) Theoretical solution

b) Gas-kinetic scheme result

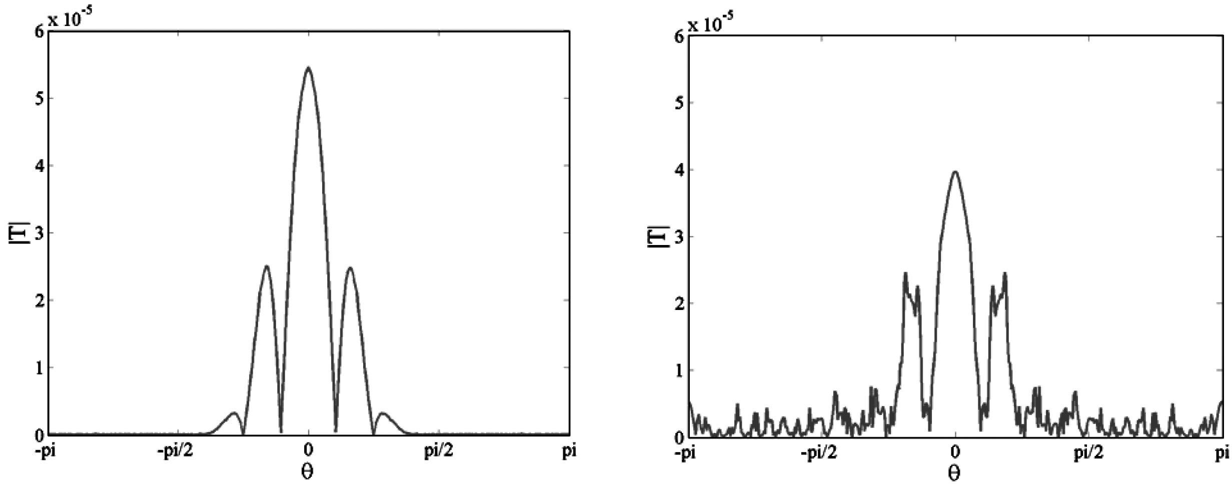

c) Theoretical solution

d) Gas-kinetic scheme result

Fig. 6 Scattered temperature field for the $\lambda = 1/3$ case. Top row: distribution of scattered temperature fluctuation amplitude $\hat{T}_s$; bottom row: circumferential variation of $\hat{T}_s$ at $r/\lambda = 7$.

incompressible isothermal flow simulations. Because a significant temperature gradient exists in the present thermal-acoustic scattering problem, the energy equation has to be included in the gas-kinetic BGK scheme. This is accomplished by making reference to the model of Su et al. [26] for low-speed flow simulations.

For a two-dimensional problem, the BGK-type model for the equilibrium distribution function in the gas-kinetic scheme can be expressed as

$$f^{\mathrm{eq}} = \rho\left(\frac{\beta}{\pi}\right)^{(K+2)/2} e^{-\beta[(\xi_x-u)^2+(\xi_y-v)^2+\boldsymbol{\zeta}^2]} \tag{33}$$

where $\beta = 1/2RT$ and $\boldsymbol{\zeta}$ is a vector in K dimensions, where K can be regarded as the implicit degree of freedom. For example, for a two-dimensional problem with diatomic gas, the explicit degree of freedom is the translational ones in the x and y directions. The corresponding implicit degrees of freedom are the translational one in the z direction and two rotational degrees of freedom for diatomic gas. Therefore, $\boldsymbol{\zeta}^2$ can be expressed as $\boldsymbol{\zeta}^2 = \zeta_1^2 + \zeta_2^2 + \cdots + \zeta_K^2$, where $K = 3$ for a two-dimensional problem with diatomic gas.

The macroscopic conservation equations in two dimensions can be derived from the modeled BE by introducing four collision invariants φ_α ($\alpha = 0, 1, 2, 3$), where $\varphi_0 = 1$, $\varphi_{1,2} = \xi$, and $\varphi_3 = (\xi_x^2 + \xi_y^2 + \boldsymbol{\zeta}^2)/2$ for the two-dimensional gas-kinetic BGK scheme, via the following equations:

$$W = \begin{pmatrix} \rho \\ \rho u \\ \rho v \\ \rho e_t \end{pmatrix} = \int \varphi_\alpha f \, \mathrm{d}\xi_x \, \mathrm{d}\xi_y \, \mathrm{d}\boldsymbol{\zeta} \tag{34}$$

The mass, momentum, and energy fluxes are obtained as follows:

$$\vec{F}(W) = \begin{pmatrix} \vec{F}_\rho \\ \vec{F}_{\rho u} \\ \vec{F}_{\rho v} \\ \vec{F}_{\rho e_t} \end{pmatrix} = \int \boldsymbol{\xi} \varphi_\alpha f \, \mathrm{d}\xi_x \, \mathrm{d}\xi_y \, \mathrm{d}\boldsymbol{\zeta} \tag{35}$$

According to Su et al. [26], the finite volume gas-kinetic BGK scheme is derived by integrating the modeled BE over the area of the numerical cell ($\mathrm{d}x\,\mathrm{d}y$) and further integrating the results with respect to time ($\mathrm{d}t$) as follows:

$$\int\left(\frac{\partial f}{\partial t} + \boldsymbol{\xi}\cdot\nabla f\right)\varphi_\alpha \, \mathrm{d}\Xi = \int\left(-\frac{f - f^{\mathrm{eq}}}{\tau}\right)\varphi_\alpha \, \mathrm{d}\Xi \tag{36}$$

where $\mathrm{d}\Xi = \mathrm{d}\xi_x \, \mathrm{d}\xi_y \, \mathrm{d}\boldsymbol{\zeta} \, \mathrm{d}x \, \mathrm{d}y \, \mathrm{d}t$. For a cell Ω with boundary $\partial\Omega$, the integral moments of f can be expressed as

$$\frac{\mathrm{d}}{\mathrm{d}t}\int_\Omega \varphi_\alpha f \, \mathrm{d}\boldsymbol{\xi} \, \mathrm{d}V + \int_{\partial\Omega} \varphi_\alpha \boldsymbol{\xi} f \, \mathrm{d}\boldsymbol{\xi} \cdot \boldsymbol{n} \, \mathrm{d}\sigma = 0 \tag{37}$$

The resulting finite volume scheme at numerical cell Ω is constructed as

$$W_\Omega^{n+1} - W_\Omega^n = \frac{1}{\Delta S_\Omega}\sum_{k=1}^{4}\int_0^{\Delta t} \vec{F}_k \cdot \vec{l}_k \, \mathrm{d}t \tag{38}$$

where ΔS_Ω is the area of the numerical cell Ω; $\Delta t = t^{n+1} - t^n$; $\vec{F}_k$ is the flux across cell interfaces normal to $\vec{k}$; and $|\vec{l}_k|$ is the length of the cell interface with normal direction $\vec{k}$. To march the macroscopic solutions from t^n to t^{n+1}, $\vec{F}_k$ in Eq. (38) should be obtained via Eq. (35); that is, the distribution function f in Eq. (35) has to be determined. The corresponding calculation method based on models developed by Su et al. [26] and Xu and He [22] will be highlighted.

A formal integral solution for the distribution function in the modeled BE is expressed in the form

$$f(\mathbf{x}, \boldsymbol{\xi}, t + \Delta t) = \frac{1}{\tau}\int_t^{t+\Delta t} f^{\mathrm{eq}}(\mathbf{x}', \boldsymbol{\xi}, t') e^{-(t+\Delta t - t')/\tau} \, \mathrm{d}t' + e^{-\Delta t/\tau} f_0(\boldsymbol{x} - \boldsymbol{\xi}\Delta t, \boldsymbol{\xi}) \tag{39}$$

where $\mathbf{x}' = \boldsymbol{x} - \boldsymbol{\xi}(t + \Delta t - t')$ is the trajectory of a particle motion. To obtain the solution of f, the f^{eq} and f_0 on the right-hand side of Eq. (39) have to be determined. Suppose there is a cell interface $x_{i+1/2}$ between two adjacent cells x_i and x_{i+1}. At the beginning of each time step Δt (assume $t = 0$ for ease of demonstration), the initial distribution function $f_0(\mathbf{x}, \boldsymbol{\xi}, t = 0)$ around $x_{i+1/2}$ can be expressed as

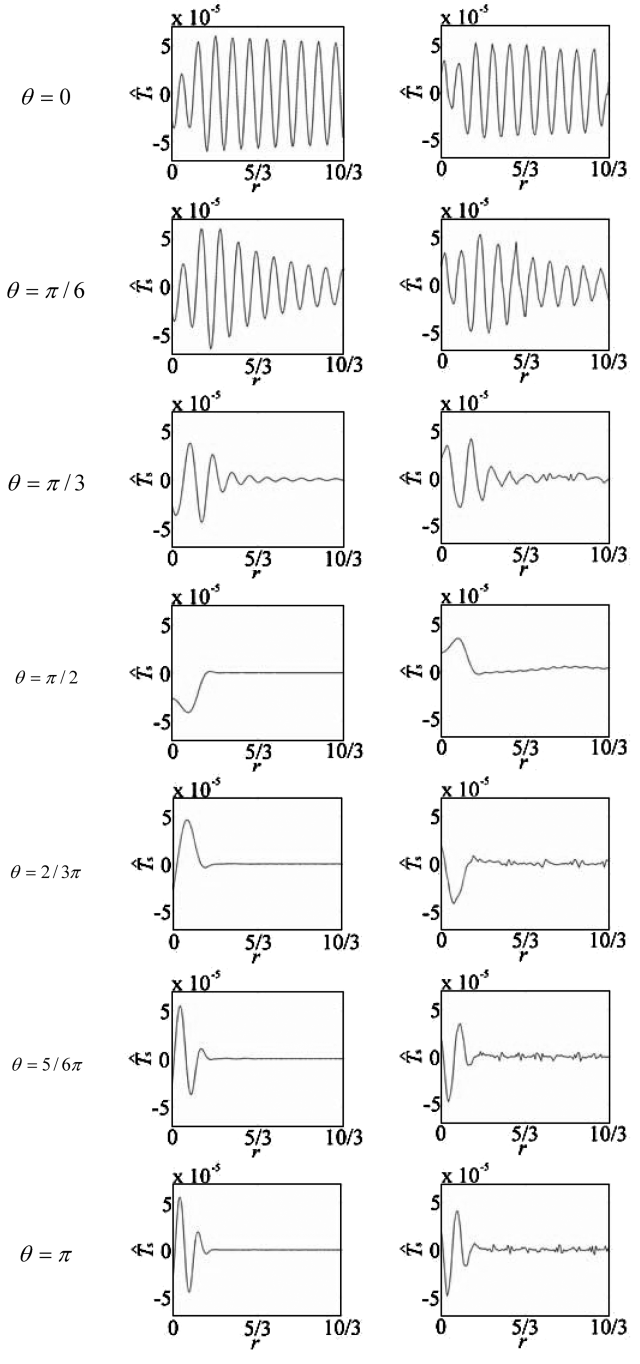

a) b)

Fig. 7 Radial variations of scattered temperature fluctuation amplitude $\hat{T}_s$ for the $\lambda = 1/3$ case ($\hat{T}_s$ against r, with $-7.5 \times 10^{-5} \le \hat{T}_s \le 7.5 \times 10^{-5}$ and $0 \le r \le 10/3$): a) theoretical solution and b) gas-kinetic scheme result.

$$
\begin{aligned}
f_0(\mathbf{x},\boldsymbol{\xi},0) &= f^{\mathrm{eq}}(\mathbf{x}_{i+1/2},\boldsymbol{\xi},0)+f^{(1)}(\boldsymbol{x}_{i+1/2},\boldsymbol{\xi},0)\\
&\quad+(x-x_{i+1/2})\cdot\nabla f^{\mathrm{eq}}(\boldsymbol{x}_{i+1/2},\boldsymbol{\xi},0)
\end{aligned}
\tag{40}
$$

where $f^{(1)}=f-f^{\mathrm{eq}}$ is defined as the nonequilibrium distribution function. To solve Eq. (40), f^{eq}, $f^{(1)}$, and the gradients of f^{eq} are calculated by following the procedure; the first step is to determine f^{eq} and its gradients, then the deviation distribution $f^{(1)}$ can be determined next. These procedures are briefly described next.

1. *Determination of* f^{eq}

The mesoscopic distribution function can be connected with the macroscopic variables by integrating the moments of f. Because of the fact that $\int -(1/\tau)(f-f^{\mathrm{eq}})\,\mathrm{d}\xi_x\,\mathrm{d}\xi_y=0$ (compatibility condition), the connection can also be made by the integral moments of f^{eq}; that is,

$$
\int \varphi_\alpha f^{\mathrm{eq}}\,\mathrm{d}\xi_x\xi_y\,\mathrm{d}\boldsymbol{\zeta}=W_{i+1/2}=(\rho\quad\rho u\quad\rho v\quad\rho e_t)^T_{i+1/2}
\tag{41}
$$

where $W_{i+1/2}$ is the macroscopic variables at cell interface $x_{i+1/2}$. According to Xu and He [22], $W_{i+1/2}$ and its gradients can be obtained from the discretized initial data W_i by a third-order central-differencing interpolation scheme; that is,

$$
W_{i+1/2}=\frac{7}{12}(W_i+W_{i+1})-\frac{1}{12}(W_{i-1}+W_{i+2})
\tag{42}
$$

$$
\left(\frac{\mathrm{d}W}{\mathrm{d}x}\right)_{i+1/2}=\left[\frac{5}{4}(W_{i+1}-W_i)-\frac{1}{12}(W_{i+2}-W_{i-1})\right]\Big/\Delta x
\tag{43}
$$

Therefore, f^{eq} is determined by substituting values from Eq. (42) into Eq. (40), using the expression of f^{eq} in Eq. (33). On the other hand, the gradients of f^{eq} are obtained by taking derivatives of Eq. (41) with values of $(\mathrm{d}W/\mathrm{d}x)_{i+1/2}$ determined from Eq. (43).

2. *Determination of* $f^{(1)}$

The next step is to determine the nonequilibrium distribution function $f^{(1)}=f-f^{\mathrm{eq}}$, which can be expressed as

$$
f^{(1)}=-\tau\left(\frac{\partial f^{\mathrm{eq}}}{\partial t}+\boldsymbol{\xi}\cdot\nabla f^{\mathrm{eq}}\right)=-\tau(a\xi_x+b\xi_y+A)f^{\mathrm{eq}}
\tag{44}
$$

where $\partial f^{\mathrm{eq}}/\partial t=Af^{\mathrm{eq}}$, $\partial f^{\mathrm{eq}}/\partial x=af^{\mathrm{eq}}$, and $\partial f^{\mathrm{eq}}/\partial y=bf^{\mathrm{eq}}$. The coefficients A, a, and b are given by $A=A_\alpha\psi_\alpha$, $a=a_\alpha\psi_\alpha$, and $b=b_\alpha\psi_\alpha$, respectively, for $\alpha=1,2,3,4$. These coefficients can be determined from

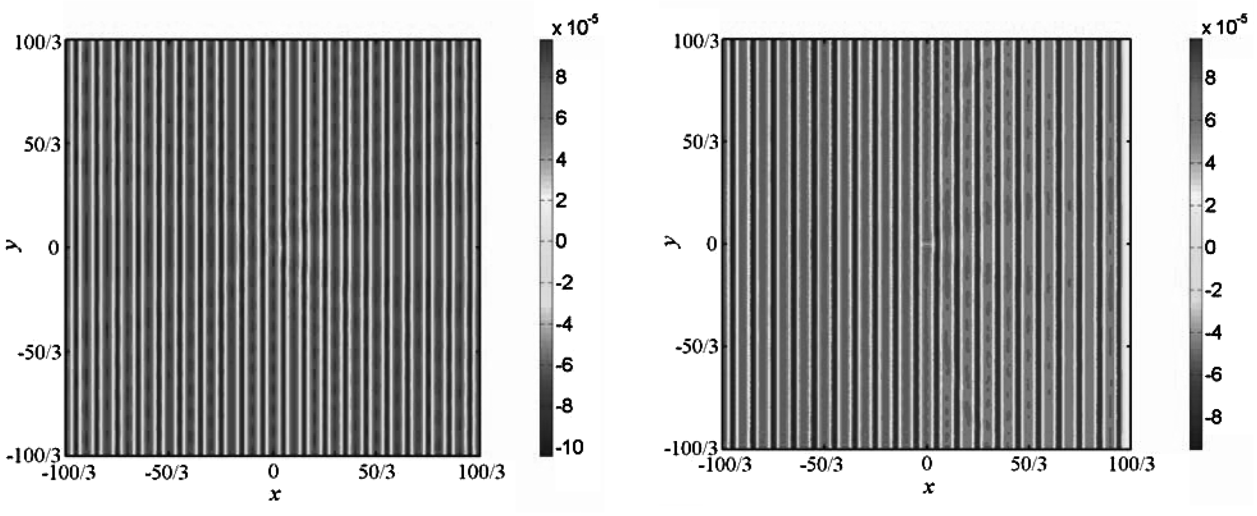

a) Theoretical solution

b) Gas-kinetic scheme result

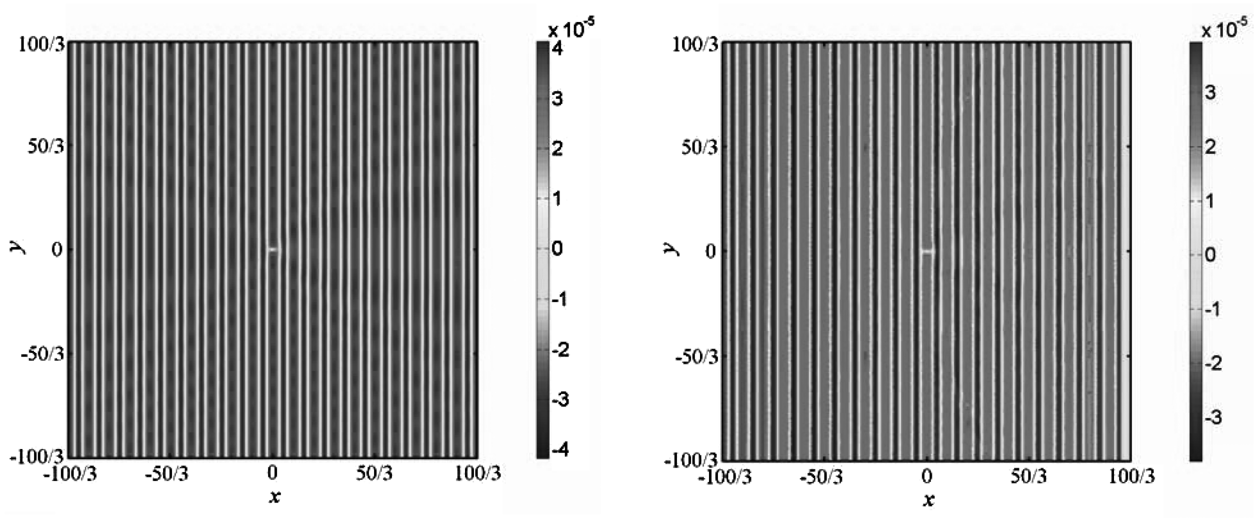

c) Theoretical solution

d) Gas-kinetic scheme result

Fig. 8 Interaction between thermal disturbance and acoustic wave for the $\lambda = 10/3$ case. Top row: total pressure fluctuation amplitude $\hat{p}$; bottom row: total temperature fluctuation amplitude $\hat{T}$.

$$\int \varphi_\alpha a f^{\mathrm{eq}}\, \mathrm{d}\xi_x \xi_y\, \mathrm{d}\varsigma = \left(\frac{\mathrm{d}W}{\mathrm{d}x}\right)_{i+1/2} \tag{45a}$$

$$\int \varphi_\alpha b f^{\mathrm{eq}}\, \mathrm{d}\xi_x \xi_y\, \mathrm{d}\varsigma = \left(\frac{\mathrm{d}W}{\mathrm{d}y}\right)_{i+1/2} \tag{45b}$$

$$\int \varphi_\alpha f^{(1)}\, \mathrm{d}\xi_x \xi_y\, \mathrm{d}\varsigma = \int -\tau \varphi_\alpha (a\xi_x + b\xi_y + A) f^{\mathrm{eq}}\, \mathrm{d}\xi_x \xi_y\, \mathrm{d}\varsigma = 0 \tag{45c}$$

$$\int \varphi_\alpha A f^{\mathrm{eq}}\, \mathrm{d}\xi_x \xi_y\, \mathrm{d}\varsigma = -\int \varphi_\alpha (a\xi_x + b\xi_y) f^{\mathrm{eq}}\, \mathrm{d}\xi_x \xi_y\, \mathrm{d}\varsigma \tag{45d}$$

Therefore, Eq. (40) becomes

$$f_0(\mathbf{x}, \boldsymbol{\xi}, t) = f^{\mathrm{eq}}[1 - \tau(a\xi_x + b\xi_y + A) + ax + by] \tag{46}$$

and the remaining unknown in Eq. (39) is f^{eq} around the cell interface $x_{i+1/2}$ at $t = 0$. This can be determined by expanding f^{eq} about $t = 0$ as

$$\begin{aligned} f^{\mathrm{eq}}(\mathbf{x}, \boldsymbol{\xi}, t) &= f^{\mathrm{eq}}(x_{i+1/2}, \xi, 0) + \frac{\partial f^{\mathrm{eq}}}{\partial x} x + \frac{\partial f^{\mathrm{eq}}}{\partial y} y + \frac{\partial f^{\mathrm{eq}}}{\partial t} t \\ &= f^{\mathrm{eq}}(1 + ax + by + At) \end{aligned} \tag{47}$$

Substituting Eqs. (46) and (47) into Eq. (39), f at cell interface $x_{i+1/2}$ becomes

$$f(\mathbf{x}_{i+1/2}, \boldsymbol{\xi}, t) = f^{\mathrm{eq}}[1 - \tau(a\xi_x + b\xi_y + A) + At] \tag{48}$$

Substituting f in Eq. (48) into Eq. (35), the mass, momentum, and energy fluxes across the cell interface $x_{i+1/2}$ can be evaluated. Marching from $t = n$ to $t = n + 1$, Eq. (38) becomes

$$\begin{aligned} W_\Omega^{n+1} = W_\Omega^n + \int_0^{\Delta t} \bigg[&\frac{1}{\Delta x}(F(W)_{i-1/2,j} - F(W)_{i+1/2,j}) \\ &+ \frac{1}{\Delta y}(F(W)_{i,j-1/2} - F(W)_{i,j+1/2}) \bigg] \mathrm{d}t \end{aligned} \tag{49}$$

Hence, the density, momentum, and energy inside the computational domain for every time step can be determined.

Time marching is based on the Courant–Friedrichs–Lewy (CFL) condition in accordance with Su et al. [26]. The ratio of the time step to the relaxation time is specified in the range of $10 \le \Delta t/\tau_{\mathrm{eff}} < 100$. The CFL number is set at 0.45 for the numerical simulation.

B. Correction for *Pr*

An attempt has been made to correct Pr for the gas-kinetic scheme [21]. However, the approach is based on numerical consideration only. In this paper, the gas-kinetic scheme adopted was modified so that Pr could be corrected by invoking the Eucken model [25].

C. Nonreflecting Boundary Conditions

The thermal-acoustic scattering problem investigated has open boundaries only; therefore, nonreflecting boundary conditions are

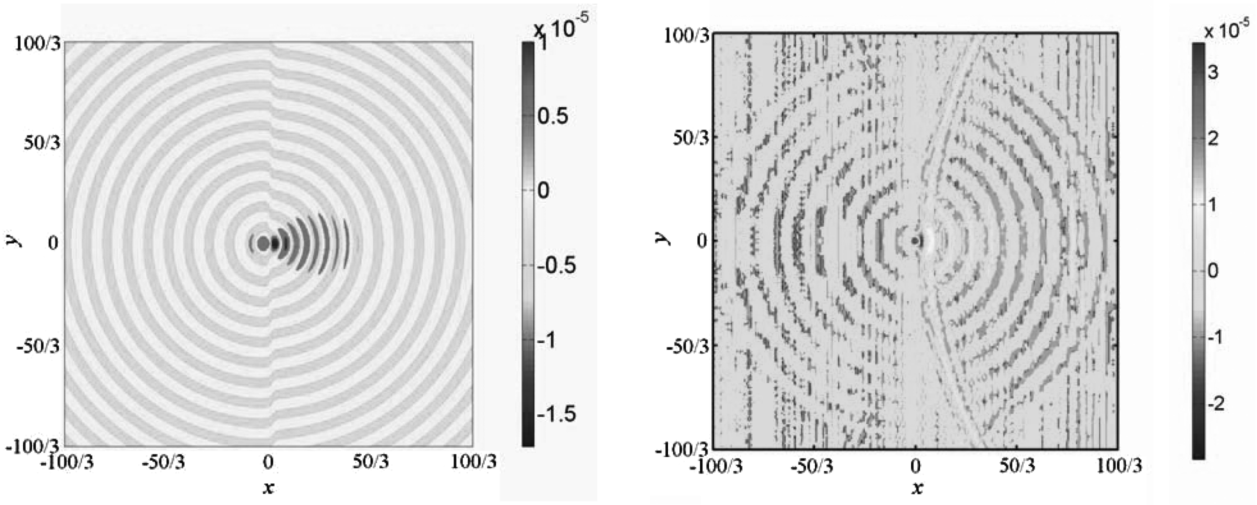

a) Theoretical solution

b) Gas-kinetic scheme result

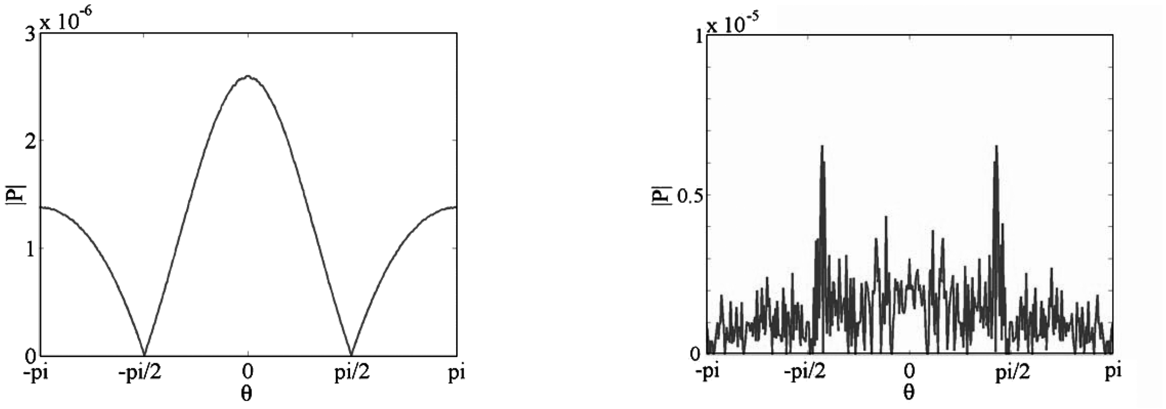

c) Theoretical solution

d) Gas-kinetic scheme result

Fig. 9 Scattered-pressure field for the $\lambda = 10/3$ case. Top row: distribution of scattered-pressure fluctuation amplitude $\hat{p}_s$; bottom row: circumferential variations of $\hat{p}_s$ at $r/\lambda = 7$.

required for its successful simulation. In principle, nonreflecting boundary conditions should be tailored for each numerical scheme. For the gas-kinetic scheme, a viable nonreflecting boundary condition based on the one-dimensional Riemann invariants is adopted for the incoming and outgoing boundaries on the left- and right-hand sides of the computational domain (Fig. 1), and a zero-order extrapolation method is applied to the upper and lower boundaries. Instead of applying the open boundary conditions to the distribution function f as in the lattice Boltzmann method [27], they are applied to the primitive variables in the gas-kinetic scheme. The corresponding f^{eq} is updated via Eq. (41) at each time step along the open boundaries.

IV. Discussion of Results

Generally speaking, for scattering of acoustic plane waves by an obstacle, be it a localized vortex [8] or a rigid cylinder [7], the resulting scattering pattern is determined by the ratio between incident wavelength λ^* (dimensional) and the characteristic length of the obstacle L (in this case, the obstacle is the thermal disturbance), which can be effectively described in terms of the Helmholtz number $H_n = kL$, where $k = 2\pi/\lambda^*$ is the wave number. Because $H_n = kL = \omega L/a_\infty$, it can be viewed as a form of dimensionless frequency for the indication of the compactness of the acoustic scattering. Therefore, one can expect, for different values of H_n, that the incident acoustic wave and the obstacle will interact differently, thus creating different directivity patterns. To show that such interaction physics also occur with the present thermal scattering problem, two limiting cases with $H_n > 1$ and $H_n < 1$, are attempted.

Because the thermal disturbance is bounded at $r = 1.0$, then $L = 3.0$. The first case is set with $H_n = 6\pi$, which gives a dimensionless wavelength $\lambda = \lambda^*/L = 1/3$, and the second case is set with $H_n = 0.6\pi$ for a dimensionless wavelength $\lambda = 10/3$. The first case can be regarded as a scattering in the short-wavelength (or high-frequency) limit or the WKB limit, and the second case can be referred to as a scattering in the long-wavelength (or low-frequency) limit or the Born limit.

The theoretical solution for the scattering problem is obtained numerically with an incident acoustic wave amplitude specified as $A = 1 \times 10^{-4}$. The center of the thermal disturbance is located at $(x, y) = (0, 0)$, as shown in Fig. 1. The radial heat distribution and the corresponding temperature and density distributions are also shown in the figure. The calculations of the two cases (with $\lambda = 1/3$ and $10/3$) are carried out by rescaling the size of the thermal disturbance. As a result, the size of the computational domain remains the same for both cases. However, the computational domain has to be big enough to allow the solution to be resolved accurately. These two cases are discussed subsequently.

A. Case 1: $\lambda = 1/3$

This case corresponds to $H_n = 6\pi$. The grid sizes are specified as $\Delta x = \Delta y = 5 \times 10^{-2}/3$, with 400×400 grid points in the computational domain. This choice is equivalent to a physical domain size of $-10/3 \leq x \leq 10/3$ and $-10/3 \leq y \leq 10/3$. The incident acoustic wave is released at $x = -10/3$. According to Morse and Uno Ingard [7], the choice of this λ is not common in acoustic scattering studies. However, it is expected that the scattering behavior would be distinct from that for the long-wavelength limit.

The theoretical and numerically simulated total pressure and temperature fluctuation amplitudes $\hat{p}$ and $\hat{T}$ of the interaction are shown in Fig. 2. Obviously, a sharp-edged shadow is created behind the thermal disturbance for this case (Figs. 2a and 2b). The presence of such a sharp-edged shadow in the forward-scattering direction (downstream direction) agrees with the general theory of acoustic scattering [7]. For this short-wavelength scattering case, the sharp-edged shadow formed behind the obstacle (thermal disturbance) results from the interaction between the scattered wave and the undisturbed plane acoustic waves behind the obstacle. The scattered wave is defined as the interfering wave, which interferes destructively with the undisturbed plane acoustic waves downstream. This interfering wave makes up half of the total scattered wave. The other half is regarded as the reflected waves, which spread out nearly uniformly in all directions. Because pressure and density are related by $\hat{p} = a_\infty^2 \hat{\rho}$, their fluctuation behavior will be essentially the same; therefore, the resulting $\hat{\rho}$ is not shown. Similar scattering patterns are also observed in the resulting temperature fluctuation $\hat{T}$, which is obtained from Eq. (4) (see Figs. 2c and 2d).

The directivity patterns of the scattered-pressure fluctuation amplitude $\hat{p}_s$ are shown in Fig. 3. In Fig. 3a, it can be clearly seen that peak scattering occurs along the axis of symmetry of the thermal disturbance, accompanied by secondary peaks approximately at angles $\theta = \pm\pi/6$ with scattering amplitudes about half of that along the axis of symmetry. The reflection of the scattered waves is not

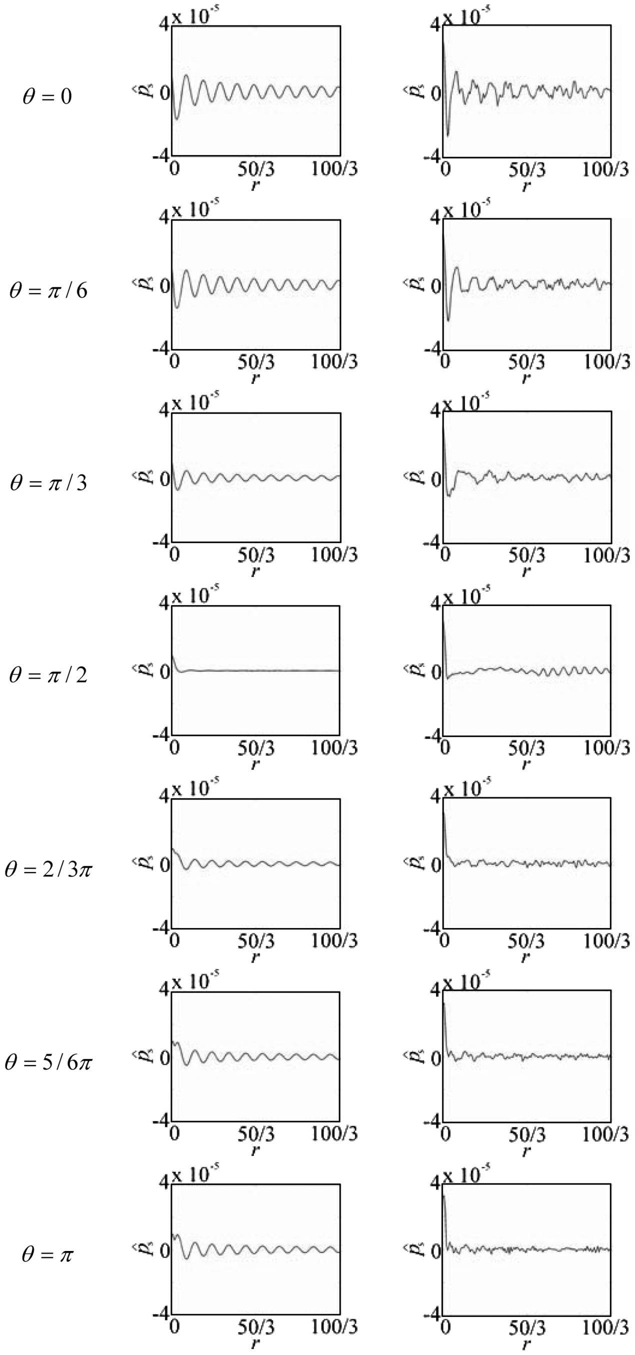

a) b)

Fig. 10 Radial variations of scattered-pressure fluctuation amplitude $\hat{p}_s$ for the $\lambda = 10/3$ case ($\hat{p}_s$ against r, with $-4 \times 10^{-5} \leq \hat{p}_s \leq 4 \times 10^{-5}$ and $0 \leq r \leq 100/3$): a) theoretical solution and b) gas-kinetic scheme result.

significant for this WKB limit. On the other hand, numerical error in the form of high-frequency oscillations is detected in Fig. 3b. This numerical error can be attributed to the fact that the nonreflecting boundary condition based on Riemann invariants is not truly nonreflecting for scattered waves with any angle of incidence approaching the outgoing boundaries. In fact, the Riemann invariants are most effective for outgoing waves that are normal to the open boundaries only. In this $\lambda = 1/3$ case, most of the scattered waves are concentrated at the wake region of the thermal disturbance. As a result, most of the scattered waves exit the outgoing boundary at small angles of incidence; this means that the Riemann invariants are approximately valid and the scattered field is not much altered by the small amount of reflected waves bouncing back from the open boundaries. However, the scattered patterns plotted in Fig. 4 show that the gas-kinetic scheme result is in good agreement with that deduced analytically.

In Figs. 2–4, the gas-kinetic scheme solutions generally show good agreement in directivity patterns with the corresponding theoretical solutions. However, the theoretically predicated and the gas-kinetic calculated amplitudes of the primary and secondary scattering peaks differ. This can be observed from the circumferential variations of fluctuation amplitude at $r/\lambda = 7$ (Fig. 3). The gas-kinetic calculations give 1.25×10^{-4} and 0.58×10^{-4} for the amplitude of the primary and secondary scattered peaks, respectively. They are smaller than the corresponding values deduced from the theoretical solution (1.38×10^{-4} and 0.62×10^{-4}). The reduction in scattered fluctuation amplitude can be explained by the nonlinear interaction between the incident acoustic waves and the distributed heat source. The modulation of the amplitude of the scattered waves, resulting from the nonlinear thermal-acoustic interaction, is revealed by this one-step aeroacoustics simulation obtained by solving the modeled BE. On the other hand, such nonlinear interaction is missing in the framework of LEE on which the present theoretical analysis is based.

The variation of the scattered-pressure amplitude $\hat{p}_s$ from $\theta = 0$ to π along radii originated from the center of the thermal disturbance is illustrated in Fig. 5. The dissection of the scattered field with respect to different θ obtained by the gas-kinetic scheme (Fig. 5b) clearly shows the modulation of scattered amplitude by the nonlinear thermal-acoustic interaction and the numerical errors detected with increasing θ, as compared with those results given by the theoretical solution (Fig. 5a).

The theoretical and calculated directivity patterns of the scattered temperature fluctuation amplitude $\hat{T}_s$ are shown in Fig. 6. The corresponding circumferential variation of the scattered amplitude from $\theta = 0$ to π along radii originated from the center of the heat source are illustrated in Fig. 7. The directivity pattern for $\hat{T}_s$ is similar to that for $\hat{p}_s$ and $\hat{\rho}_s$ (not shown). However, the order of magnitude of the scattered temperature is 10^{-5}, which is 10^{-4} times the temperature variation of the thermal disturbance (where the thermal difference within the distributed heat source has an order of magnitude of 10^{-1}). Again, the alteration of the scattered amplitude due to the nonlinear thermal-acoustic interaction is replicated as that shown by $\hat{p}_s$ and $\hat{\rho}_s$, with numerical error detected starting at $\theta \geq \pi/6$ for the gas-kinetic scheme (Fig. 7) compared with the theoretical results. Again, the discrepancy between the gas-kinetic scheme solution and the theoretical result can be attributed to the inefficiency of the nonreflecting boundary conditions toward the outgoing waves with large angle of incidence ($\theta \geq \pi/6$). The directivity pattern for the short-wavelength limit is found to be similar to that of sound scattering by a vortex pair composed of two Oseen vortices of opposite circulation [28]. However, no details of the theoretical derivation of the corresponding sound-scattering problem was given in their paper; therefore, a quantitative comparison is not possible at this time.

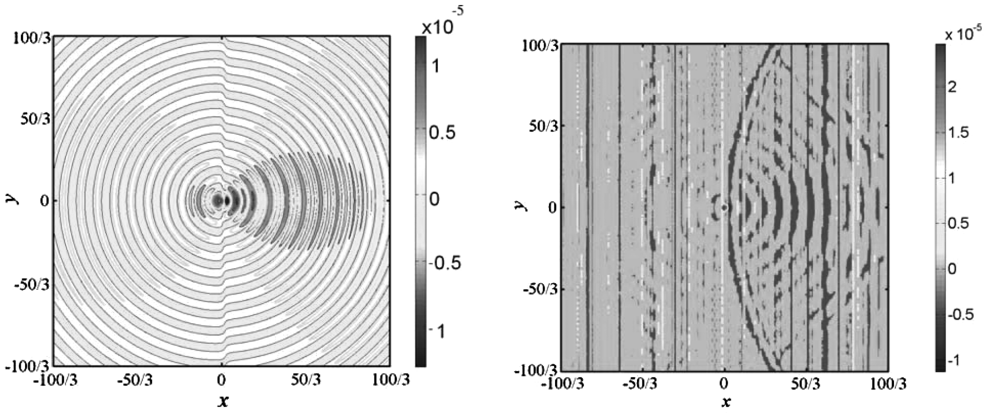

a) Theoretical solution

b) Gas-kinetic scheme result

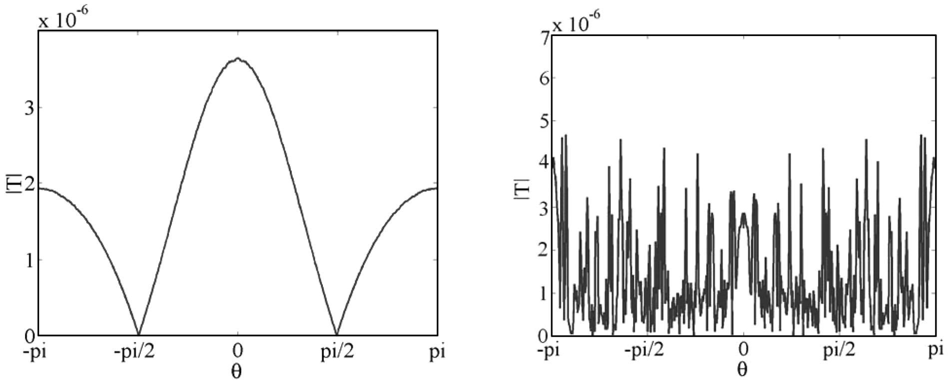

c) Theoretical solution

d) Gas-kinetic scheme result

Fig. 11 Scattered temperature field for the $\lambda = 10/3$ case. Top row: distribution of scattered temperature fluctuation amplitude $\hat{T}_s$; bottom row: circumferential variation of $\hat{T}_s$ at $r/\lambda = 7$.

B. Case 2: $\lambda = 10/3$

This case corresponds to $H_n = 0.6\pi$. In this case the grid sizes chosen are given by $\Delta x = \Delta y = 5 \times 10^{-2}/3$ and again a 400×400 grid is located inside the computational domain. After rescaling the distributed heat source size by $1/10$ times that for case 1, the computational domain represents a physical domain with size given by $-100/3 \le x \le 100/3$ and $-100/3 \le y \le 100/3$. The incident acoustic wave is specified at $x = -100/3$. In this case, the radius of the distributed heat source is about 0.3 times the incident acoustic wavelength and can be regarded as the long-wavelength limit (i.e., the Born limit). According to Morse and Uno Ingard [7], acoustic scattering in the Born limit is of strong practical interest and is thus studied extensively.

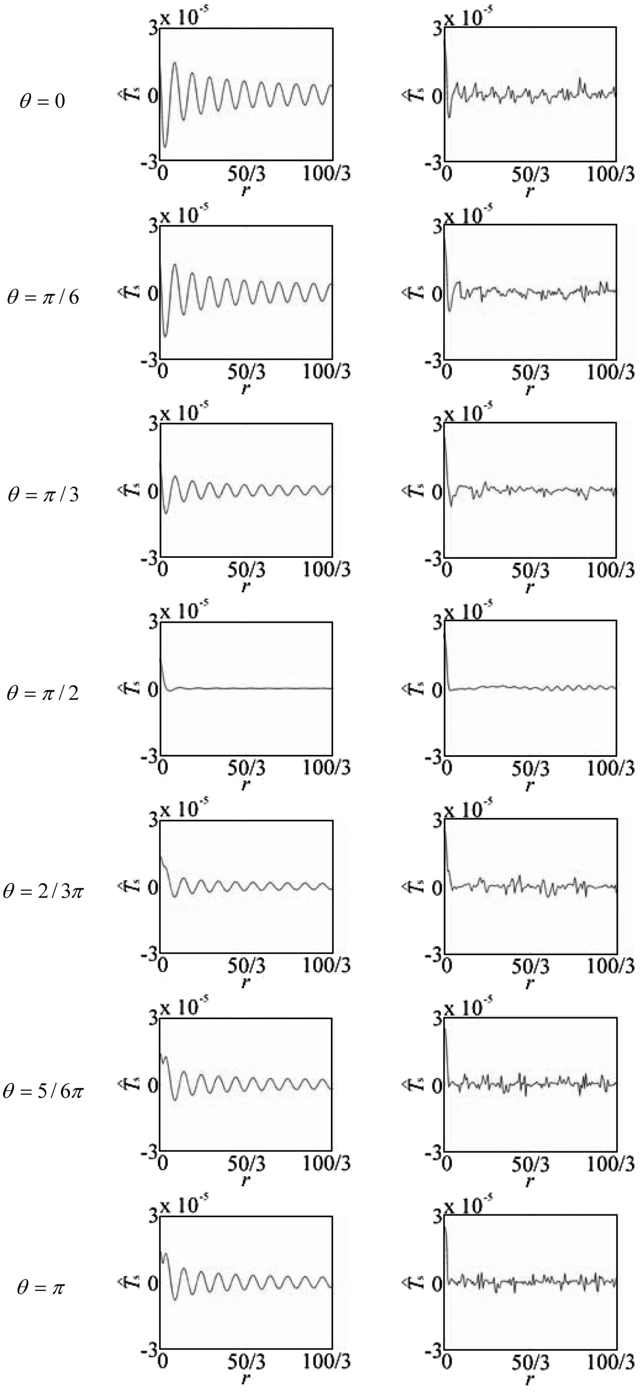

a) **b)**

Fig. 12 Radial variations of scattered temperature fluctuation amplitude $\hat{T}_s$ for the $\lambda = 10/3$ case ($\hat{T}_s$ against r, with $-3 \times 10^{-5} \le \hat{T}_s \le 3 \times 10^{-5}$ and $0 \le r \le 100/3$): a) theoretical solution and b) gas-kinetic scheme result.

Unlike case 1, the scattered waves spread out in all directions as reflected waves. Because the interfering wave is negligible in this long-wavelength limit, no sharp-edged shadow is expected in the scattered field. The corresponding contours of the resulting pressure $\hat{p}$ and temperature $\hat{T}$ fluctuation are shown in Fig. 8. It can be seen from the figures that the fluctuations are quite uniform.

The scattered pressure $\hat{p}_s$ and the corresponding directivity pattern are shown in Fig. 9. As can be seen from Fig. 9a, the scattered pressure spreads more or less uniformly in all directions, with the peak amplitude at the immediate wake region of the distributed heat source. No shape-edged shadow is detected; instead, the scattered waves spread out more or less uniformly at about $-7\pi/18 \le \theta \le 7\pi/18$. As shown in Fig. 9b for the scattered pressure $\hat{p}_s$, the fundamental behavior of the scattered field is replicated by the gas-kinetic scheme. However, significant reflection of the scattered waves is detected and captured in the calculated scattered-pressure distribution in Fig. 9b.

As shown in the theoretical solution (Fig. 9c), there is a phase change at $\theta = \pm\pi/2$. Maximum amplitude is reported at $\theta = 0$ and decreases to its minimum at $\theta = \pm\pi/2$ and increases again to its secondary peak at $\theta = \pi$. This indicates that the reflected portion of the scattered wave is significant for this long-wavelength or Born limit. Again, a significant reflection of the scattered waves is detected and captured in the directivity plot in Fig. 9d. Because the scattered waves enclose a much wider angle ($-7\pi/18 \le \theta \le 7\pi/18$) compared with case 1, the angle of incidence for the scattered wave exiting the open boundaries is much larger than that found in case 1. Therefore, Riemann invariants are not sufficient to guarantee true nonreflecting boundary conditions for the scattered waves, and the scattered field is therefore superimposed by the reflected waves from the boundaries. As a result, the fundamental behavior of the scattered pattern can be recognized but the amplitude of the scattered waves is contaminated by numerical noise. The phenomenon is revealed clearly by the variation of $\hat{p}_s$, with θ ranging from 0 to π along radii originated from the center of the thermal disturbance (Fig. 10).

The scattered temperature $\hat{T}_s$ is obtained from Eq. (4). The corresponding directivity plots and scattered patterns are shown in Fig. 11. Again, the scattered waves deduced from the theoretical solution (Figs. 11a and 11c) spread out uniformly with maximum amplitude around $\theta = 0$ with a drop at $\theta = 0$. There is a noticeable phase change at $\theta = \pm\pi/2$. The scattered amplitude decreases to its minimum at $\theta = \pm\pi/2$ and increases again to its secondary peak at $\theta = \pi$. Similar to the explanation for the scattered pressure and density, there is significant reflection of scattered waves for this long-wavelength-limit case. Again, the scattering pattern can be seen from the distribution of the scattered temperature $\hat{T}_s$, and the scattered waves are superimposed with numerical noise, as shown in Fig. 11d. The same phenomenon can be seen from the variation of $\hat{T}_s$, with θ ranging from 0 to π along radii originated from the center of the thermal disturbance (Fig. 12). On the other hand, the numerical errors due to the gas-kinetic scheme are even more significant compared with those in case 1, because the scattered magnitude in case 1 is approximately 10^{-4}, whereas it is around 10^{-6} in this case. As a result, poor agreement is obtained between the theoretical and the gas-kinetic solutions for this case.

V. Conclusions

Acoustic scattering by a thermal disturbance with zero net heat gain/loss has been studied. A theoretical solution has been derived and used as a benchmark problem to verify the validity and extent of the gas-kinetic scheme for direct aeroacoustid simulation. The thermal disturbance is so structured that a steady-state solution can be obtained for this acoustic scattering problem. Two cases [namely, the short wavelength ($\lambda = 1/3$) or WKB limit and the long wavelength ($\lambda = 10/3$) or Born limit] are investigated theoretically and numerically by solving the modeled BE using a gas-kinetic scheme. Different scattered patterns are obtained for both limits, which is a consequence of the difference in scattered waves resulting from the interaction between the incident sound waves and the localized thermal disturbance.

For the $\lambda = 1/3$ case, a shadow with a sharp edge is observed behind the thermal disturbance along its x axis of symmetry in the forward-scattering direction, whereas it is absent in the $\lambda = 10/3$ case. The difference is clearly shown on the directivity plots, where reflection is insignificant for the $\lambda = 1/3$ case, whereas it is important for the $\lambda = 10/3$ case.

For the $\lambda = 1/3$ case, the gas-kinetic simulation results show good agreement with the theoretical solutions. Also, the nonlinear thermal-acoustic interaction between the thermal disturbance and the incident acoustic waves are appropriately resolved by this one-step aeroacoustic simulation, whereas the corresponding thermal-acoustic interaction is not considered in the analytical solutions or in any other two-step numerical schemes for aeroacoustic simulations. The computational boundaries based on Riemann invariants are sensitive to the angle of incidence of the exiting waves. Because the scattered waves are concentrated in the wake region of the thermal disturbance, most of the scattered waves are exiting the nonreflecting boundaries with small angles of incidence. Therefore, both the scattered pattern and the amplitudes are preserved, and the discrepancy in scattered amplitudes between the gas-kinetic simulation results and the theoretical solutions could be attributed to the different physics embodied in the assumptions of the two approaches.

For the $\lambda = 10/3$ case, due to the large obliqueness of the scattered waves propagating toward the exiting boundaries, only the basic scattered pattern is reproduced, whereas the scattered amplitudes cannot be compared with those obtained from theoretical analysis, as they are contaminated by the reflected waves from the open boundaries. These results show that for the $\lambda = 10/3$ case, the Riemann-invariant boundary conditions are not appropriate and need improvement.

Acknowledgments

Support received from the Research Grants Council of the Government of the Hong Kong Special Administrative Region through grants PolyU1/02C, PolyU5303/03E, and PolyU5232/04E and through grants A-PA5U and A-PA9Y from Hong Kong Polytechnic University (HKPolyU) is gratefully acknowledged. The first author (E. W. S. Kam) would like to give her heartfelt thanks to Christopher K. W. Tam for his guidance on deriving the theoretical solutions during her academic visit at the Department of Mathematics, Florida State University, with support from Out-Going Research Student Attachment Programme 2007 from HKPolyU.

References

[1] Trilling, L., "On Thermally Induced Sound Fields," *Journal of the Acoustical Society of America*, Vol. 27, No. 3, 1955, pp. 425–431. doi:10.1121/1.1907920

[2] Colonius, T., and Lele, S. K., "Computational Aeroacoustics: Progress on Nonlinear Problems of Sound Generation," *Progress in Aerospace Sciences*, Vol. 40, No. 6, 2004, pp. 345–416. doi:10.1016/j.paerosci.2004.09.001

[3] Colonius, T., Lele, S. K., and Moin, P., "Boundary Conditions for Direct Computation of Aerodynamic Sound Generation," *AIAA Journal*, Vol. 31, No. 9, 1993, pp. 1574–1582. doi:10.2514/3.11817

[4] Li, X. M., Leung, R. C. K., and So, R. M. C., "One-Step Aeroacoustics Simulation Using Lattice Boltzmann Method," *AIAA Journal*, Vol. 44, No. 1, 2006, pp. 78–89. doi:10.2514/1.15993

[5] Georges, T. M., "Acoustic Ray Paths through a Model Vortex with a Viscous Core," *Journal of the Acoustical Society of America*, Vol. 51, No. 1b, 1972, pp. 206–209. doi:10.1121/1.1912831

[6] Müller, E. A., and Matschat, K. R., "The Scattering of Sound by a Single Vortex and by Turbulence," U.S. Air Force Office of Scientific Research, Rept. AFOSR-TN-59-337, Wright–Patterson AFB, OH, 1959.

[7] Morse, P. M., and Uno Ingard, K., *Theoretical Acoustics*, McGraw–Hill, New York, 1968.

[8] Colonius, T., Lele, S. K., and Moin, P., "The Scattering of Sound Waves by a Vortex: Numerical Simulations and Analytical Solutions," *Journal of Fluid Mechanics*, Vol. 260, No. -1, 1994, pp. 271–298. doi:10.1017/S0022112094003514

[9] Ford, R., and Llewellyn Smith, S. G., "Scattering of Acoustic Waves by a Vortex," *Journal of Fluid Mechanics*, Vol. 386, 1999, pp. 305–328. doi:10.1017/S0022112099004371

[10] Ferziger, J. H., "Low-Frequency Acoustic Scattering from a Trailing Vortex," *Journal of the Acoustical Society of America*, Vol. 56, No. 6, 1974, pp. 1705–1707. doi:10.1121/1.1903502

[11] O'Shea, S., "Sound Scattering by a Potential Vortex," *Journal of Sound and Vibration*, Vol. 43, No. 1, 1975, pp. 109–116. doi:10.1016/0022-460X(75)90209-6

[12] Howe, M. S., "Contributions to the Theory of Aerodynamic Sound, with Application to Excess Jet Noise and the Theory of the Flute," *Journal of Fluid Mechanics*, Vol. 71, No. 4, 1975, pp. 625–673. doi:10.1017/S0022112075002777

[13] Yates, J. E., "Application of the Bernoulli Enthalpy Concept to the Study of Vortex Noise and Jet Impingement Noise," NASA CR 2987, 1978.

[14] Candel, S. M., "Numerical Solution of Wave Scattering Problems in the Parabolic Approximation," *Journal of Fluid Mechanics*, Vol. 90, No. 3, 1979, pp. 465–507. doi:10.1017/S0022112079002354

[15] Mawardi, O. K., "Aero-Thermoacoustics—The Generation of Sound by Turbulence and by Heat Processes," *Reports on Progress in Physics*, Vol. 19, No. 1, 1956, pp. 156–187. doi:10.1088/0034-4885/19/1/305

[16] Bass, H. E., "Absorption of Sound by Air: High Temperature Prediction," *Journal of the Acoustical Society of America*, Vol. 69, No. 1, 1981, pp. 124–138. doi:10.1121/1.385356

[17] Rijke, P. L., "Notiz über Eine Neue Art, Die in Einer an Beiden Enden Offenen Röhre Enthaltene Luft in Schwingungen zu Versetzen," *Annalen der Physik*, Vol. 183, No. 6, 1859, pp. 339–343.

[18] Rayleigh, J. W. S., *The Theory of Sound*, Dover, New York, 1945.

[19] Landa, P. S., *Nonlinear Oscillations and Waves in Dynamical Systems*, Kluwer Academic, Dordrecht, The Netherlands, 1996.

[20] Farouk, B., Oran, E. S., and Fusegi, T., "Numerical Study of Thermoacoustic Waves in an Enclosure," *Physics of Fluids*, Vol. 12, No. 5, 2000, pp. 1052–1062. doi:10.1063/1.870360

[21] Xu, K., "A Gas-Kinetic BGK Scheme for the Navier–Stokes Equations, and Its Connection with Artificial Dissipation and Godunov Method," *Journal of Computational Physics*, Vol. 171, No. 1, 2001, pp. 289–335. doi:10.1006/jcph.2001.6790

[22] Xu, K., and He, X. Y., "Lattice Boltzmann Method and Gas-Kinetic BGK Scheme in the Low-Mach Number Viscous Flow Simulations," *Journal of Computational Physics*, Vol. 190, No. 1, 2003, pp. 100–117. doi:10.1016/S0021-9991(03)00255-9

[23] Chu, B. T., "On the Energy Transfer to Small Disturbances in Fluid Flow (Part 1)," *Acta Mechanica*, Vol. 1, No. 3, 1965, pp. 215–234. doi:10.1007/BF01387235

[24] Abramowitz, M., and Stegun, I. A., *Handbook of Mathematical Functions*, Dover, New York, 1965.

[25] Leung, R. C. K., Kam, E. W. S., and So, R. M. C., "Recovery of the Transport Coefficients in the Navier–Stokes Equations from the Modeled Boltzmann Equation," *AIAA Journal*, Vol. 45, No. 4, 2007, pp. 737–739. doi:10.2514/1.29265

[26] Su, M., Xu, K., and Ghidaoui, M. S., "Low-Speed Flow Simulation by the Gas-Kinetic Scheme," *Journal of Computational Physics*, Vol. 150, No. 1, 1999, pp. 17–39. doi:10.1006/jcph.1998.6162

[27] Kam, E. W. S., Leung, R. C. K., and So, R. M. C., "Lattice Boltzmann Method Simulation of Aeroacoustics and Non-Reflecting Boundary Conditions," *AIAA Journal*, Vol. 45, No. 7, 2007, pp. 1703–1712. doi:10.2514/1.27632

[28] Berthet, R., and Astruc, D., "Numerical Boundary Conditions for Sound Scattering Simulation," *Journal of Computational Physics*, Vol. 190, No. 1, 2003, pp. 64–99. doi:10.1016/S0021-9991(03)00254-7

J. Astley
Associate Editor